Unsupervised Sparse Pattern Diagnostic of Defects with Inductive Thermography Imaging System

Bin Gao, *Senior Member IEEE*, W.L. Woo, *Senior Member*, *IEEE*, Yunze He, *Member IEEE*, G.Y. Tian, *Senior Member, IEEE*,

***Abstract* — This paper proposes an unsupervised method for diagnosing and monitoring defects in inductive thermography imaging system. The proposed method is fully automated and does not require manual selection from the user of the specific thermal frame images for defect diagnosis. The core of the method is a hybrid of physics-based inductive thermal mechanism with signal processing-based pattern extraction algorithm using sparse greedy based Principal Component Analysis (SGPCA). An internal functionality is built into the proposed algorithm to control the sparsity of SGPCA. and to render better accuracy in sizing the defects. The proposed method is demonstrated on automatically diagnosing the defects on metals and the accuracy of sizing the defects. Experimental tests and comparisons with other methods have been conducted to verify the efficacy of the proposed method. Very promising results have been obtained where the performance of the proposed method is very near to human perception.**

***Index Terms* — Data analytics for diagnosis and monitoring, instrumentation, inductive thermal imaging, machine intelligence, non-destructive testing and evaluation.**

I. Introduction

Imaging diagnostic system for defect detection is highly demanded in industry [1, 2]. This has been applied on inspection of electronic chips or dies in semiconductor production lines [3]. Acciani *et al.* extracted the features of the regions of interest in test images and then built multilayer neural networks for defect detection [4] on solder joints in surface mount technology of industry. Tsai *et al.* proposed defect inspection system of solar modules in electroluminescence (EL) images [5]. A. Picon *et al.* proposed fuzzy spectral and spatial feature integration method for classification of nonferrous materials in hyperspectral data [6]. All these methods recognize that image based defect diagnostic system is a wide group of analysis technique used in science and industry to evaluate the properties of material, component or system without causing damage [7-9]. Infrared thermography systems have reached a prominent status as a nondestructive testing and evaluation (NDT&E) image diagnostic method [10-12] with the advantages of being fast, and providing non-contact, non-interaction, real-time measurements over a large detection area with a long range, security of personnel, and relatively easy interpretation of results. Infrared thermography can be used to assess and predict the structure or behavior beneath the surface by measuring the distribution of infrared radiation and converting the measurements into a temperature scale.

Inductive thermography (IT) system which combines two techniques: Eddy Current (EC) and thermography [13] has the potential with an increasing span of applications [14]. Comparing with other thermography NDT&E systems, the heat of IT is not limited to the sample surface, rather it can reach a certain depth, which governed by the skin depth of eddy current. Furthermore, IT focuses the heat on the defect due to friction or eddy current distortion, which increases the temperature contrast between the defective region and defect-free areas. Eddy current pulsed thermography (ECPT) is a kind of IT methods which is the most widely used such as penetration depths measurement in metallic materials [15], small defects detection for compressor blades [16], probability of detection (POD) estimation [17] of fatigue cracks, impact evaluation in carbon fibre reinforced plastic (CFRP) [18], corrosion and blister detection under coating [19] and multiple cracks detection [20]. All these works require signal processing tools to do defects analysis. In ECPT, several thermal transient response features have been used as an indicator of defect status, which is critical for acceptance/rejection decisions for maintenance and lifetime prediction [21]. Most methods are limited on manually selecting the proper contrast components. To enhance the flaw contrast and improve noise rejection qualities, pattern based image enhancement has been conducted by introducing the raw data upon a set of orthogonal basis functions. Fourier transform was applied to pulsed thermography, and enhanced the flaw-contrast significantly using phase map [22]. Influence of non-uniform heating and surface emissivity variation was removed by using a Fourier transformation based image reconstruction algorithm [23]. Instead of a prescribed set of basis functions, empirical orthogonal functions were also employed to maximize the anomalous patterns of transient response. The efficiency of Principal Component Analysis (PCA) was compared on thermography features extraction by considering the initial sequence as either a set of images or a set of temporal profiles [24]. In addition, the Independent Component Analysis (ICA) [25, 26] and Non-negative Matrix Factorization (NMF) [27, 28] are proposed for defect characterization in IT system. However,

Manuscript received on 06 November 2014

Bin Gao is with the School of Automation Engineering, University of Electronic Science and Technology of China, China. (e-mail:bin_gao@uestc.edu.cn)

W.L. Woo is with the School of Electrical and Electronic Engineering, Newcastle University, UK. (e-mail: w.l.woo@ncl.ac.uk)

Yunze He is with the College of Mechatronics Engineering and Automation, National University of Defense Technology (NUDT), China (e-mail: hejicker@163.com)

G. Y. Tian is with the School of Automation Engineering, University of Electronic Science and Technology of China, China, and also with the School of Electrical and Electronic Engineering, Newcastle University, UK. (e-mail: g.y.tian@ncl.ac.uk)

most pattern extraction based methods are only employed as a signal processing tool. The physics mechanism is not fully linked to provide the benefits on defect detection and while the results are acceptable, they are not completely accurate. This ambiguous case prevents the use of IT system in automated environments.

The sparse modeling of signals [29-36] which has proven to be effective in signal processing, denoising, deconvolution, compressive sensing reconstruction, inpainting, data mining, multimedia, nonnegative matrix factorization and etc. Most natural signals exhibit such sparsity property in adequately chosen signal representations. These include the wavelets [37], the curvelets [38] or even adaptively learned signal representations [39]. Greedy algorithms [40] have been widely used to find approximate solutions quickly to combinatorial optimization problems [41]. In a few cases, optimal solutions are guaranteed. Greedy algorithms for sparse approximation have inspired less adaptive methods. Matching pursuit (MP) can be converted to a low complexity adaptive form, as done in [42], and been extended to orthogonal MP (OMP) [43] as well as stage-wise OMP [44]; Compared with convex relaxation algorithms, greedy pursuits need more measurements, but they tend to be more computationally efficient. Sparsity has been exploited in recent unsupervised pattern recognition methods [45-48]. The group of research interest focuses on the low-rank and sparse components via convex optimization have also been attractive, the robust PCA, is [49] proposed iterative thresholding methods with low complexity, but with low speed of convergence. Lin *et al.* [50] proposed accelerated proximal gradient (APG) methods which are faster and more accurate than robust PCA. The latest approach such as variational Bayesian and Markov chain Monte Carlo (MCMC) based sparse PCA with specific prior where the model parameters and hyperparameters are adapted by using the [51, 52]. In all cases, a fully Bayesian treatment is applied to inference. While these approaches increase the accuracy of specific application and works efficient when suitable prior is selected. Moreover, it consumes significantly high computational complexity at each iteration to adapt the parameters and its hyperparameters.

The contributions of the current work lie in the development of the physics mechanism that underlies the IT system and a derivation of a mathematical model that bridges the gap between the physics mechanism and signal processing analysis. The aim is to develop a data-analytics algorithm to extract anomalous patterns in the IT system. A physics-based signal processing approach combining sparse greedy Principal Component Analysis (SGPCA) is developed to identify and search the defect region in the sample. The model represents a low-rank variable as a sparse bilateral factorization with greedy-based optimization to reduce the computational complexity during the sparse pattern extraction stage. The physics mechanism as to why sparse information benefits the IT heating phase will also be discussed in details. The comparison in terms of the probability of detection and computational complexity has been undertaken for different sparse pattern extraction algorithms through the real experiments. Experimental tests on man-made metal defects and natural defects with complex geometry have been conducted to show the validity of the proposed algorithm.

The paper is organized as follows: Section II discusses the physics model of IT mechanism and the linkage as well as development of sparse pattern extraction algorithm. Section III describes the proposed sparse thermal pattern extraction method. Sections IV and V introduce the experimental setup and present the experiment results. Finally, Section VI concludes the work.

II. PROPOSED METHODOLOGY

Physics Mechanism of Inductive Thermography System

1) Inductive Thermal Conduction

The infrared camera records both the spatial and the transient response of temperature variation on the specimen. This can be represented as a spatial-transient tensor $\bar{\mathbf{Y}}$ which has dimension $\underbrace{N_x \times N_y}_{\text{Spatial}} \times \underbrace{N}_{\text{Transient}}$. The governing equation describing the EM field in the ECPT system can be deduced from Maxwell's equations. When an EM field is applied to a conductive material, the temperature increases owing to resistive heating from the induced electric current which is known as Joule heating. The sum of the generated resistive heat Q is proportional to the square of the magnitude of the electric current density. Current density, in turn, is proportional to the electric field intensity vector $\vec{E}$. The following equation expresses this relationship:

$$Q = \frac{1}{\sigma}\left|\vec{J}_s\right|^2 = \frac{1}{\sigma}\left|\sigma\vec{E}\right|^2 \quad \text{where} \quad \sigma = \frac{\sigma_0}{1+\alpha\left(T-T_0\right)} \tag{1}$$

σ is dependent on temperature, and σ_0 is the conductivity at the reference temperature T_0 and α is the temperature coefficient of resistivity, which describes how resistivity varies with temperature. In general, by taking account of heat diffusion and Joule heating [24], the heat conduction equation of a specimen can be expressed as:

$$\frac{\partial T}{\partial t} = \frac{k}{\rho C_p}\left(\frac{\partial^2 T}{\partial x^2}+\frac{\partial^2 T}{\partial y^2}+\frac{\partial^2 T}{\partial z^2}\right)+\frac{1}{\rho C_p}q\left(x,y,z,t\right) \tag{2}$$

where $T = T\left(x,y,z,t\right)$ is the temperature distribution, k is the thermal conductivity of the material (W/m K), which is dependent on temperature. ρ is the density (kg/m^3), C_p is specific heat (J/kg K). $q\left(x,y,z,t\right)$ is the internal heat generation function per unit volume, which is the result of the eddy current excitation. The variation of temporal temperature depends on the spatial temperature variation for heat conduction. According to Eqn. (2), heat conduction is influenced by $T\left(x,y,z,t\right)$, ξ, υ, σ, μ, and l. Here ξ denotes the sensor geometry factor; υ denotes the parameters of the excitation (frequency, amplitude, etc.) and l denotes the

lift-off (distance between the sensor and sample). From the above analysis, it becomes clear that the variation of temperature spatially and its transient response recorded from the IR camera directly reveals the intrinsic properties variation of the conductive material.

2) Inductive Thermography Defect Detection

Fig. 1 shows the diagram of inductive thermography defect detection system. The excitation signal generated by the excitation module is a small period of high frequency current. The current in the coil will induce the eddy currents and generate the resistive heat in the conductive material. The heat will diffuse in time until the heat reaches equilibrium in the material. If a defect (e.g. crack, fatigue region) is present in the conductive material, eddy current distribution as well as heat diffusion process will vary. Consequently, the spatial distribution of temperature on the surface of material and the temperature transient response will show the variation, which is captured by an infrared camera. It can be divided into two phases: heating phase and cooling phase. As an example, we take a finite length sample with small penetrated slot as a defect testing sample. The resultant heating frame from IT (0.1s) is presented in Fig. 1 right bottom panel. In the heating phase, different heat generation rates enlarge the temperature spatial variation. Hot spots are observed around the slot tips and the cool areas locate at both sides of the slot. In the cooling phase, heat diffuses from high temperature area to low temperature area, and reduces the contrast. In addition, the area where locate far away from excitation coil will continually rising temperature because of heat diffusion. These different areas can be considered as the pattern regions which share the similar transient responses in the sample. The infrared camera functioned as a temperature spatial image signal recorder along with time flowing. In addition, the camera actually records the mixed image signal corresponding to the signal image from the thermal pattern regions at each time point. These regions are termed as thermal patterns in inductive thermography.

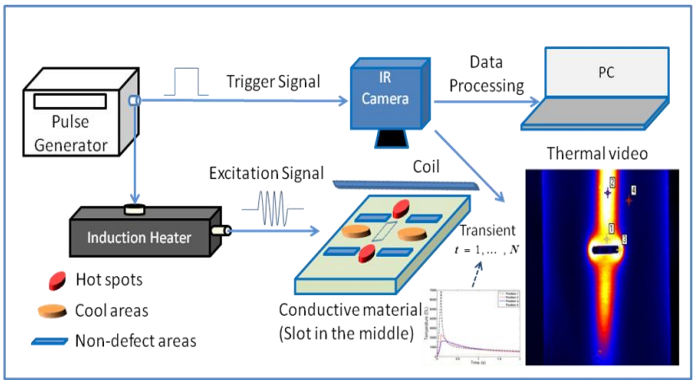

Fig. 1: ECPT system.

The hot spots are used specially for defect location and sizing. Fig. 1 shows the example of temperature distribution at the sample surface as the lift-off distance is set d = 4mm. When the inductor is close to the tip of the defect (d = 4 mm), it is seen that significant eddy current flows around the tip of the defect and the defect behaves predominantly as a slot.

3) Relationship between excitation system, heating phase and cooling phase with respect to material variation

IT uses inductive heater as the excitation system. Hence, it is specific for conductive materials or multi-layer system with conductive layer. The inductive heat depends on the parameters of material and excitation signal. 1) To optimize the signal-to-noise ratio (SNR), the heat power should be maximized. Normally, the high current amplitude (hundreds of ampere) and great frequency (>100 kHz) are used. 2) The longer heating time results in the accumulation of large amount of heat *Q*. For detecting surface defects, the long heating time is useful for good SNR and contrast [18]. At the same time, the longer heating time is useful for detecting the deep defects due to heat conduction from surface to deep defects [51]. 3) The long cooling time is useful for heat conduction to detect deep defects. The thermal penetration depth for a pulsed excitation is determined by the thermal diffusivity α of the material and by the observation time *t* (cooling time) after pulse heating. 4) The small electrical conductivity can lead to a high heat power and great eddy current penetration depth. The thermal diffusivity depends on thermal conductivity, mass density and specific heat. If the thermal diffusivity is large, the temperature changes quickly. Hence the sampling frequency of the camera must be high enough to capture the changes of temperature.

4) Detectability

In general, the ECPT is valid for both deep and shallow defects, which is based on the physics principles of inductive heating, heat conduction, and infrared radiation. According to skin effect in inductive heating, the eddy current has a penetration depth δ , which is expressed by equation $\delta = \frac{1}{\sqrt{f \pi \mu \sigma}}$ where *f* is the frequency of the pulsed excitation. If the shallow defects are in this skin area, they will disturb the eddy current distribution and then temperature distribution. Theoretically, the lower excitation frequency has deeper detection depth. In practice, in order to improve the heating efficient with inductive thermography, the frequency is about 100 kHz and the skin depth is relative small. For example, ferromagnetic metals have a much smaller skin depth (about 0.04mm at 100 kHz). Therefore, shallow/surface defects can be detected. 2) The heat will conduct to the interior and lateral area of the material. If the deep defects disturb the heat conduction process, the surface temperature distribution will be different from the surrounding area. The heat conduction is used to detect the deep defects [51]. 3) The temperature will be captured by IR camera. If the surface defects show a different emissivity value, the temperature will be different from the surrounding area.

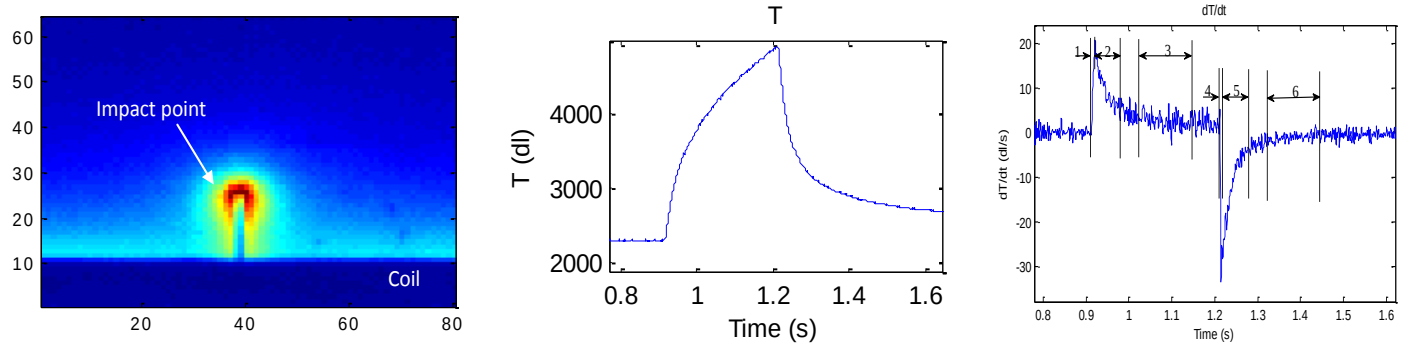

(a) (b) (c)

Fig. 2: (a) Thermal image at 0.1s after heating, (b) transient temperature response at impact point plotted against time, (c) 1st derivatives of temperature response

5) Inductive thermography multi-phase analysis

According to (2), the 1st order derivative of the temperature response of transient response, as shown in Fig. 2(b), is composed of heat diffusion and Joule heating [52]. In Fig. 2(c), we can infer from the thermal video that the heat conduction procedure can be divided into six phases:

- Phase 1: A resultant singular electric current field is generated, and the eddy current quickly rises from zero to maximum, and then converges to a steady state. This phase is very short (approximately 5ms) and the heat diffusion does not play an obvious role which can be considered zero or a constant small value. In Eqn. (2), we only take into account the Joule heating during this phase.
- Phase 2: Electric current field maintains a stable state. The sum of the generated resistive heat Q is constant. However, heat diffusion velocity gradually increases and following a different temperature increase according to Fourier's law of heat conduction. Simultaneously, heat diffusion is getting more obvious due to the significant heating propagation time. Heat diffusion plays a main role in the thermal video during this phase.
- Phase 3: Heat conduction also reaches the equilibrium state. The sum of the generated resistive heat Q and heat diffusion are at equilibrium in this phase.
- Phase 4: Eddy current quickly decreases from maximum to zero when exciting signal is stopped. Similar to the first phase, the procedure is very short, which lasts about 5ms. Change of heat diffusion is not abrupt in such a short time. Joule heating plays a main role in the thermal video during this phase.
- Phase 5: There is no eddy current in this phase, so $q(x, y, z, t)$ can be omitted in Eqn. (2). The change of the 1st order derivative is resulted from the velocity variation of heat diffusion.
- Phase 6: Heat diffusion is at a stable state.

As mentioned in the Introduction, IT focuses the heat on the defect due to friction and eddy current distortion, which increases the temperature contrast. Thus, for surface defects, the selection of phase one and four are directly attributed to Joule heating due to the eddy current distortion. More description and comparison of phase selection will be detailed in Section V. Moreover, the IR camera used as a temperature measurement sensor has an important role in inductive thermography. Inductive thermograph is a relative measurement technique, the temperature contrast between defect and surrounding area is important. Therefore, the sensitivity of camera has an influence on defect detect sensitivity. In the proposed method, the high end thermal camera is used, the SC7500 is a Stirling cooled camera with a 320×256 array of 1.5-5um InSb detectors. This camera has a sensitivity of $<$ 20 mK and a maximum full frame rate of 383 Hz such that the interface of the camera sensitivity can be reduced to minima. The distance has an influence on the heating efficiency. A small distance is desirable, but with an overly too small distance, the distribution of the eddy current is forced into a small area, which reduces the detectable area. To avoid this effect, transmission mode where IR camera and heater are located on the opposite side of objects is investigated if the object is thin. The increase of distance may decrease the SNR and defect detectability. In the proposed method, the 1 mm distance lift-off between the coil and sample is verified to balance good SNR and proper excitation heating.

III. Physics-Based Data Analytics

Thermography Sparse Pattern Extraction

1) Observation Model

As shown in Fig. 1, hot spots are observed around the slot tips and the cool areas locate at both sides of the slot. In the cooling phase, heat diffuses from high temperature area to low temperature area, and reduces the contrast. In addition, the area where locate far away from excitation coil will continually rising temperature because of heat diffusion. These different areas can be considered as the thermal pattern regions. Specifically, it can be seen in Fig. 1, position 1 represents an hot spots region $\mathbf{X}_1(t)$ with high rising and high falling rate of temperature; position 2 represents an cool areas $\mathbf{X}_2(t)$ with moderate rising and falling rate; position 3 represents an non-defect region $\mathbf{X}_3(t)$ with high rising rate followed by a continually low speed rising and then drop down; and position 4

represents an non-excitation region $\mathbf{X}_4(t)$ with continually temperature increasing. Mathematically, the thermography image captured by the infrared camera is considered as a mixing observation signal image $\mathbf{Y}(t)$. The term m_i is the mixing parameter which describes the contribution of the i^{th} position to the induced recorded thermography image in Fig. 1. Thus, the mathematical model [25] can be described as:

$$\mathbf{Y}(t) \approx \sum_{i=1}^{N_s} m_i \mathbf{X}_i(t) \tag{3}$$

where N_s denotes the number of independent signal image areas. The visual representation of Eqn. (3) is shown in Fig. 3.

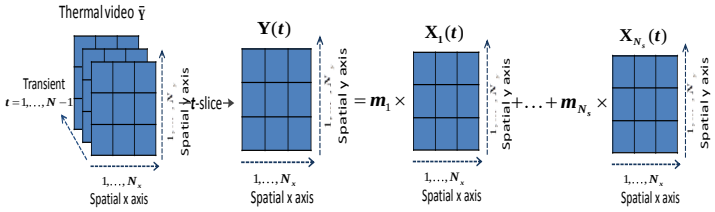

Fig. 3: Mathematical representation of mixing process of ECPT

Our previous study [25] has developed single channel blind source separation algorithm for pattern separation of inductive thermography. However, the method requires statistical independence on the waveform within the duration of signal capture and further process of pattern identification is also demanded which is often violated in practice. Instead, we use a fixed-length segment drawn from transient response [53, 54], such that continuous transient slices of length N can be chopped out of a set of image sequences from t to $t+N-1$, and the subsequent segment is denoted as $\mathbf{Y}' = \left[\text{vec}(\mathbf{Y}(t)), \text{vec}(\mathbf{Y}(t+1)), \ldots, \text{vec}(\mathbf{Y}(t+N-1))\right]^{\mathbf{T}}$ where ' $\mathbf{T}$ ' denotes the transpose operator and ' vec ' denotes the vectorize operator. The constructed image sequences is then expressed as a linear combination of the signals generated by the different pattern regions such that

$$\mathbf{Y}' = \mathbf{M}\mathbf{X}' \tag{4}$$

where $\mathbf{Y}' \in R^{N \times L}$, $L = N_x \times N_y$. $\mathbf{M} = \left[\mathbf{m}_1, \ldots, \mathbf{m}_{N_s}\right] \in R^{N \times N_s}$ is the mixing matrix, $\mathbf{m}_i$ is the i^{th} mixing vector and $\mathbf{X}' = \left[\text{vec}(\mathbf{X}_1(t)), \text{vec}(\mathbf{X}_2(t)), \ldots, \text{vec}(\mathbf{X}_{N_s}(t))\right]^{\mathbf{T}} \in R^{N_s \times L}$. Assuming that $N_s = N$ and $\mathbf{M}$ has full rank.

2) General Principle of Pattern Extraction

Our previous study already used general PCA to separate the observed variables. To solve Eqn. (4), one possible way is to use the singular value decomposition (SVD) which is a form of factorization

$$\mathbf{Y}' = \mathbf{U}\mathbf{\Sigma}\mathbf{V} \tag{5}$$

where $\mathbf{U}$ and $\mathbf{V}$ are the orthogonal matrices and $\mathbf{\Sigma}$ consist of the singular values. The columns of $\mathbf{U}$ represent the PCA basis vectors. With possible dimension reduction, e.g. choosing $N_s \le N$, there exits N_s number of basis vectors maximally informative subspace of input data, thus the basis vectors are selected and determined by the information contained in the nonzero singular values.

3) Sparse Pattern Extraction

However, previous study does not involve or leverage on the phases of heat conduction and sparse factors. Sparseness refers to a representational scheme where only a few units (out of a large population) are effectively used to represent typical data vectors [55]. In effect, this implies most units taking values close to zero while only few take significantly non-zero values. The sparse factors enforce the solution to consider only the significant region where the defect may lie within the surrounding background. This is shown in Fig. 2(a). For data with sparse outliers or partially contaminated by noise of overwhelming magnitude, sheer low-rank assumption cannot fully capture its complex structure. Therefore, (4) can be considered as combination of sparse pattern (e.g. hot spots) and non-sparse patterns

$$\mathbf{Y}' = \underbrace{\left[\mathbf{M}\mathbf{X}'\right]_{i=1,\ldots,N_s, i\neq j}}_{\mathbf{L}} + \underbrace{\mathbf{M}_j\mathbf{X}'_j}_{\mathbf{S}} + \mathbf{G} \tag{6}$$

In reality, they play an important role in enhancing the defect detectability of IT system. A general assumption of Eqn. (6) can be denoted as $\mathbf{Y}' = \mathbf{L} + \mathbf{S} + \mathbf{G}$, i.e., the pattern matrix $\mathbf{Y}'$ can be decomposed as the sum of a low-rank matrix $\mathbf{L}$ (e.g. for position 2, 3 and 4 reflected patterns in Fig. 1), a sparse pattern $\mathbf{S}$ (e.g. hot spots) which contains the spiky anomalies that are rarely shared by different instances, and $\mathbf{G}$ which is the noise term. When the algorithm optimizes the sparse $\mathbf{S}$, it is actually trying to find the joint sparse estimation of $\mathbf{M}_j$ and $\mathbf{X}'_j$ (not just $\mathbf{X}'_j$). The sparse estimation of $\mathbf{X}'_j$ is required to obtain the correct shape of the pattern while the sparse estimation of $\mathbf{M}_j$ is to enable the user to determine the exact time when the target pattern takes place. By replacing $\mathbf{L}$ with its bilateral factorization $\mathbf{L} = \mathbf{U}\mathbf{V}$ where $\mathbf{U}$ and $\mathbf{V}$ are rank-1 matrices of Eqn. (6) (The low-rank matrix variable in solving other thermal patterns is modeled in a bilateral factorization form $\mathbf{UV}$ for the purpose of developing SVD-free algorithms.) and regularizing the L_1- norm of $\mathbf{S}$ entries, the cost function can be expressed as:

$$\min_{\mathbf{U},\mathbf{V},\mathbf{S}} \left\|\mathbf{Y}' - \mathbf{U}\mathbf{V} - \mathbf{S}\right\|_F^2 + \lambda \left\|\text{vec}(\mathbf{S})\right\|_1 \tag{7}$$

where $\text{vec}(\cdot)$ denotes the vectorize operation, $\|\cdot\|_F$ denotes the Frobenius norm and $\|\cdot\|_1$ denotes L_1-norm. In this paper, we explore the greedy pursuit model [56] for optimizing the parameters in Eqn. (7). The advantage of this method is that it can significantly balance both complexity and accuracy. By optimizing $\mathbf{U}, \mathbf{V}, \mathbf{S}$, we take the gradient of the cost function with respect to these parameters and set it to 0. Starting with $\mathbf{U}$, we have

$$\frac{\partial\left\|\mathbf{Y}'-\mathbf{UV}-\mathbf{S}\right\|_F^2+\lambda\left\|\mathrm{vec}(\mathbf{S})\right\|_1}{\mathbf{U}}=\left(\mathbf{Y}'-\mathbf{UV}-\mathbf{S}\right)\mathbf{V}^{\mathbf{T}}$$
$$\left(\mathbf{Y}'-\mathbf{UV}-\mathbf{S}\right)\mathbf{V}^{\mathbf{T}}=0$$
$$\left(\mathbf{Y}'-\mathbf{S}\right)\mathbf{V}^{\mathbf{T}}-\mathbf{UVV}^{\mathbf{T}}=0 \quad (8)$$
$$\mathbf{U}_k=\left(\mathbf{Y}'-\mathbf{S}\right)\mathbf{V}_{k-1}^{\mathbf{T}}\left(\mathbf{V}_{k-1}\mathbf{V}_{k-1}^{\mathbf{T}}\right)^{-1}$$

Note subscript in *k* denotes the variable in the k^{th} iterate. Next, we consider **V**:

$$\frac{\partial\left\|\mathbf{Y}'-\mathbf{UV}-\mathbf{S}\right\|_F^2+\lambda\left\|\mathrm{vec}(\mathbf{S})\right\|_1}{\partial\mathbf{V}}=\mathbf{U}^{\mathbf{T}}\left(\mathbf{Y}'-\mathbf{UV}-\mathbf{S}\right)$$
$$\mathbf{U}^{\mathbf{T}}\left(\mathbf{Y}'-\mathbf{UV}-\mathbf{S}\right)=0$$
$$\mathbf{U}^{\mathbf{T}}\left(\mathbf{Y}'-\mathbf{S}\right)-\mathbf{VU}^{\mathbf{T}}\mathbf{U}=0 \quad (9)$$
$$\mathbf{V}_k=\left(\mathbf{U}_{k-1}^{\mathbf{T}}\mathbf{U}_{k-1}\right)^{-1}\mathbf{U}_{k-1}^{\mathbf{T}}\left(\mathbf{Y}'-\mathbf{S}\right)$$

Finally, we consider **S**:

$$\frac{\partial\left\|\mathbf{Y}'-\mathbf{UV}-\mathbf{S}\right\|_F^2+\lambda\left\|\mathrm{vec}(\mathbf{S})\right\|_1}{\partial\mathbf{S}}=\left(\mathbf{Y}'-\mathbf{UV}-\mathbf{S}\right)+\lambda$$
$$\left(\mathbf{Y}'-\mathbf{UV}-\mathbf{S}\right)+\lambda=0 \quad (10)$$
$$\mathbf{S}_k=\mathbf{S}_\lambda\left(\mathbf{Y}'-\mathbf{U}_k\mathbf{V}_k\right)$$

where in (10), $\mathbf{S}_\lambda$ is an element-wise soft thresholding operator with λ threshold such that $\mathbf{S}_\lambda\mathbf{Y}'=\left\{\mathrm{sgn}\left(\mathbf{Y}'_{mn}\right)\max\left(\left|\mathbf{Y}'_{mn}\right|-\lambda,0\right)\right\}$. In this work, λ is selected by exploring the heuristic approach to get the optimal threshold. We will treat this in two cases. For the case where **S** is positive, the differentiation of abs(**S**) results in unity. This allows λ to be incorporated into the solution to render extraction of sparse pattern. For the special case of **S** is zero, even though this point is non-differentiable, it is does not prevent the development of the proposed algorithm. The reason is because at this point (**S** = **0**), the image is already sparse and there is no further need to impose lambda into the solution.

For computation efficiency [57], we investigate the product of $\mathbf{U}_k\mathbf{V}_k$,this leads to $\mathbf{U}_k\mathbf{V}_k=\mathbf{U}_k\left(\mathbf{U}_k^{\mathbf{T}}\mathbf{U}_k\right)^{-1}\mathbf{U}_k^{\mathbf{T}}\left(\mathbf{Y}'-\mathbf{S}\right)=P_{\mathbf{U}_k}\left(\mathbf{Y}'-\mathbf{S}\right)$. This implies that the product $\mathbf{U}_k\mathbf{V}_k$ equals to the orthogonal projection of $\left(\mathbf{Y}'-\mathbf{S}\right)$ onto the column space of $\mathbf{U}_k$. According to (8), the column space of $\mathbf{U}_k$ can be represented by arbitrary orthonormal basis for the columns of $\left(\mathbf{Y}'-\mathbf{S}\right)\mathbf{V}_{k-1}^{\mathbf{T}}$, For example, we can compute it as $\mathbf{Q}$ via fast *QR* decomposition $\mathbf{QR}=QR\left(\left(\mathbf{Y}'-\mathbf{S}\right)\mathbf{V}_{k-1}^{\mathbf{T}}\right)$. In this case, the product $\mathbf{U}_k\mathbf{V}_k$ can be equivalently computed as $\mathbf{U}_k\mathbf{V}_k=P_{\mathbf{Q}}\left(\mathbf{Y}'-\mathbf{S}\right)=\mathbf{QQ}^{\mathbf{T}}\left(\mathbf{Y}'-\mathbf{S}\right)$. Therefore, $\mathbf{U}_k$ and $\mathbf{V}_k$ in (8) can be replaced by $\mathbf{Q}$ and $\mathbf{Q}^{\mathbf{T}}\left(\mathbf{Y}'-\mathbf{S}\right)$, respectively. This gives a faster updating procedure. In addition, the proposed method invokes the updates in (8) with a greedy incremental rank *r* for both **U** and **V**. In particular, it starts from a $\mathbf{V}\in\Re^{r_0\times N}$ with a small integer r_0, iterates (8) and (9) for *K* times, and then augment the rank of **V** to $r_1=r_0+\Delta r$ by adding Δr extra rows to **V**, where Δr is the rank step size. In the proposed model, the Δr rows are selected greedily as the top Δr row basis on which the object decreases fastest. Accordingly, they maximizes the magnitude of the partial derivative of the object with respect to **UV**, which is basis on which the object decreases fastest. Namely,

$$\frac{\partial\left\|\mathbf{Y}'-\mathbf{UV}-\mathbf{S}\right\|_F^2}{\partial\mathbf{V}}=\mathbf{Y}'-\mathbf{UV}-\mathbf{S} \quad (11)$$

Hence the Δr rows are the top Δr right singular vectors of the fat matrix $\mathbf{U}^{\mathbf{T}}\left(\mathbf{Y}'-\mathbf{UV}-\mathbf{S}\right)$, which can be quickly obtained by a small SVD and The rank *r* stops augmenting when reaching certain error tolerance. In the proposed model, the top r_i row basis are successfully obtained when optimizing **V** of $r_i+\Delta r$ rows. The essential task of the updates is to optimize the added Δr rows, while the first r_i rows take part in the update merely for keep the incoherence between rows. Therefore, it converges faster than simultaneously optimizing the whole *r* rows. In addition, the newly added Δr rows are initialized as the fastest decreasing directions. This repeatedly increases the rank until a sufficiently small decomposition error is achieved. The rank of the low-rank component is adaptively estimated and does not rely on initial estimation. The specific steps can be summarized in Table I.

TABLE I: THERMAL SPARSE PATTERN EXTRACTION

Input: matrix representation of first derivative of ECPT thermal video $\mathbf{Y}'$ (Inductive phase one is selected)
rank step size Δr; power K;tolerance τ; sparse term λ
Output: thermal low rank pattern **UV** and sparse pattern **S**
Procedure:
Initialize: $\mathbf{V}\in\Re^{r_0\times N}$ and **S**
while *residual error* < τ
for *k=1: K*
$\mathbf{U}_k=\mathbf{Q}, QR\left(\left(\mathbf{Y}'-\mathbf{S}_{k-1}\right)\mathbf{V}_{k-1}^{\mathbf{T}}\right)=\mathbf{QR}$
$\mathbf{V}_k=\mathbf{Q}^{\mathbf{T}}\left(\mathbf{Y}'-\mathbf{S}_{k-1}\right)$
$\mathbf{S}_k=\mathbf{S}_\lambda\left(\mathbf{Y}'-\mathbf{U}_k\mathbf{V}_k\right)$
end
Calculate the top Δr right singular vectors $\boldsymbol{\upsilon}$
of $\frac{\partial\left\|\mathbf{Y}'-\mathbf{UV}-\mathbf{S}\right\|_F^2}{\partial\mathbf{V}}=\mathbf{Y}'-\mathbf{UV}-\mathbf{S}$
Set $\mathbf{V}:=[\mathbf{V},\boldsymbol{\upsilon}]$
end

IV. EXPERIMENT SETUP

A. Inductive Thermography Experimental Platform

The experimental setup is shown in Fig. 4(a). An Easyheat 224 from Cheltenham Induction Heating is used for coil

excitation. The Easyheat has a maximum excitation power of 2.4 kW, a maximum current of 400 A_{rms} and an excitation frequency range of 150-400 kHz (380 $A_{rms,}$ and power is about 2.17 kW, and 256 kHz are used in this study). The system has a quoted rise time (from the start of the heating period to full power) of 5ms, which was verified experimentally. Water cooling of coil is implemented to counteract direct heating of the coil. The IR camera, SC7500 is a Stirling cooled camera with a 320 × 256 array of 1.5-5μm InSb detectors. This camera has a sensitivity of $<$ 20 mK and a maximum full frame rate of 383 Hz, with the option to increase frame rate with windowing of the image. A rectangular coil is constructed to apply directional excitation. This coil is made of 6.35 mm high conductivity hollow copper tube. In the experiment, only one edge of the rectangular coil is used to stimulate eddy current to the underneath sample. In this study, the frame rate is 383 Hz, and 2 s videos are recorded in the experiments.

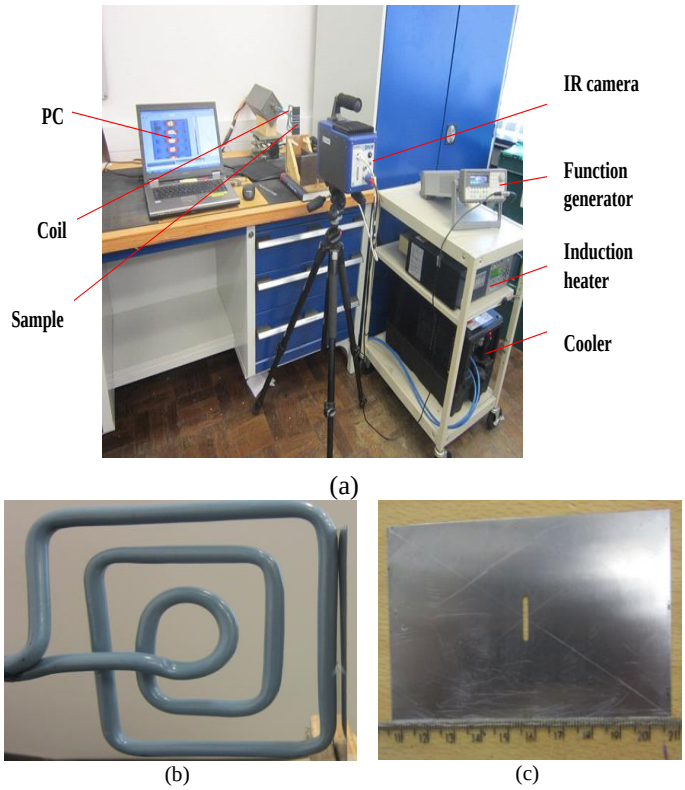

(a)

(b)

(c)

Fig. 4: (a) Inductive thermography system (b) Excitation coil (c) steel test sample

A steel sample (0.24 mm × 45 mm × 100 mm) with a slot of 10 mm length, 2 mm width is prepared (Fig. 4c). A 100 ms heating duration is selected for inspection, which is long enough to elicit an observable heat pattern. To simulate the lift-off variation in complex geometrical sample test, the steel sample is placed with a small angle against the coil (Fig. 4b).

B. Probability of defect detection

The probability of detection (POD) of defect is defined as:

$$POD = \frac{TP}{TP + FN} \tag{12}$$

where TP refers to true positive which represent the situation where the sample contains a defect and the method indicates a defect is present, and FN refers to false negative which represents the situation where the sample does not contain a defect and the method does not indicate a defect is present.

To validate the comparison results, structural similarity (SSIM) index measurement system is employed to measure the POD. It is a new index of image similarity measure. The structural similarity theory presents that natural image signals are highly structured, the structure has a very strong correlation between pixels, and especially the spatial correlation of pixel is closest. The structural similarity theory contains important information of an object structure in a visual scene. Indeed, the three components are combined to yield an SSIM given by

$$S(x,y) = f\left(l(x,y), c(x,y), s(x,y)\right) \tag{13}$$

where luminance comparison of two image (x,y) is defined as

$$l(x,y) = \frac{2u_x u_y + C_1}{u_x^2 + u_y^2 + C_1} \tag{14}$$

where u is mean intensity, C_1 is constant to avoid instability when $u_x^2 + u_y^2$ is very close to zero. The contrast comparison is defined as

$$c(x,y) = \frac{2\sigma_x\sigma_y + C_2}{\sigma_x^2 + \sigma_y^2 + C_2} \tag{15}$$

where σ is standard deviation, and the structure comparison function is defined as

$$s(x,y) = \frac{2\sigma_{xy} + C_3}{\sigma_x\sigma_y + C_3} \tag{16}$$

where σ_{xy} is correlation coefficient, C_2 and C_3 functions as same as C_1, by combing all three factors, this gives the definition of SSIM [58], namely

$$SSIM(x,y) = \frac{\left(2u_x u_y + C_1\right)\left(2\sigma_{xy} + C_2\right)}{\left(u_x^2 + u_y^2 + C_1\right)\left(\sigma_x^2 + \sigma_y^2 + C_2\right)} \tag{17}$$

V. RESULTS AND DISCUSSION

A. Influence of Phase Selection of Inductive Thermography

One example of raw inductive thermal image is shown in Fig. 1. The first derivative of transient response according (2) is shown in Fig. 5.

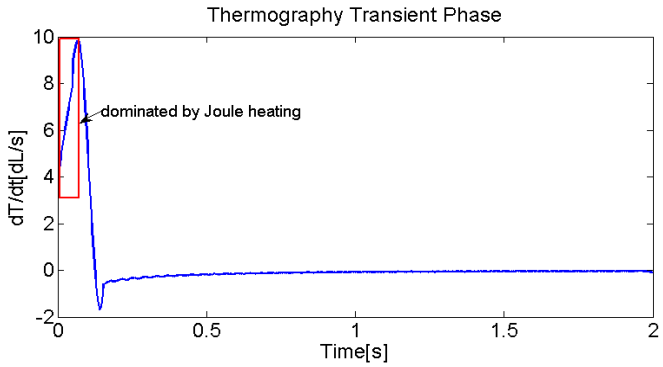

Fig. 5: First-order derivative of the transient response.

As can be seen clearly, the phase one can be interpreted within the rectangular box. In order to emphasize the importance of analyzing the phase selection, the comparison of defect pattern extraction by selecting first derivative of whole and partially (phase one) thermal video using general principle component analysis (PCA) using Eqn. (5) by setting the number N_s of pattern basis to four. This selection is based on Monte Carlo approach where the process is repeated over 100 realizations within the range between the one up to ten components and the selection of the four in order to obtain the optimal defect pattern extraction results.

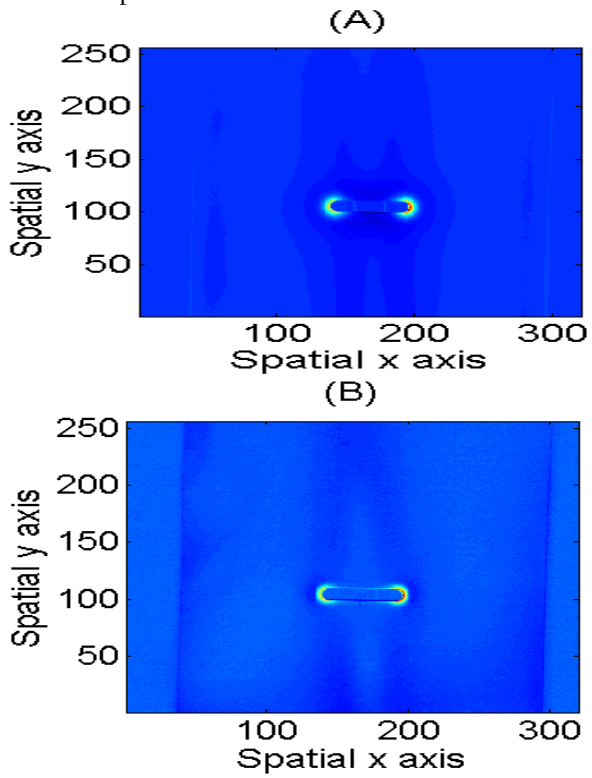

Fig. 6: (A) PCA of first derivative of whole thermal video; (B) PCA of first derivative of partially (phase one) thermal video.

In Fig. 6, both extraction results highlight the singular pattern around the crack tips. However, the PCA of first-order derivative of the "phase one" of the thermal video has enabled a heightened state of emphasis with higher resolution in the zone around the tips of the hot spots. In addition, this brings the benefit of lesser computations since only few thermal images are used. From the physics viewpoint, during the heating phase for a finite uniform thickness plate, a heat generation rate Q can be defined as the generated heat in unit time due to Joule heating, using the Cartesian coordinates (x, y) in Eqn. (18):

$$Q = \sigma\left\{\left(\frac{\partial\phi}{\partial x}\right)^2 + \left(\frac{\partial\phi}{\partial y}\right)^2\right\} \tag{18}$$

where ϕ denotes the electric potential, and σ electric conductivity. Since the two components of the electric current are expressed in terms of the derivatives of ϕ, heat generation rate Q theoretically goes to infinity at the crack tips. A resultant high temperature rising rate is generated in heating phase (i.e. crack tips) [25]. In the cooling phase, since there is no heating source, the variation of temperature T_{emp} in a finite uniform thickness plate is described by Eqn. (19).

$$\frac{\partial T_{emp}}{\partial t} = \frac{k}{\rho C_p}\left(\frac{\partial^2 T_{emp}}{\partial x^2} + \frac{\partial^2 T_{emp}}{\partial y^2}\right) \tag{19}$$

where t, ρ, C_p and k denotes time, mass density, heat capacity, and thermal conductivity, respectively. It is clear that the temporal variation of temperature depends on the variation of spatial temperature. Fourier's law of heat conduction states that the time rate of heat transfer through a material is proportional to the negative gradient in the temperature and to the cross section area of the material. For a uniform thickness plate used in this study, the cross section area is constant. Due to the singular areas around the slot tips, a high temperature gradient is generated while high eddy current density appears around the slot tips. During the shot time, the eddy current quickly rises from zero to maximum, retains at the steady state [25]. The heat diffusion does not play an obvious role as can be considered zero or a small value. This is the reason Fig. 6 indicates that the separated defect pattern place more emphasis on the crack tips where the heat diffusion does not significantly affect the heat distribution. Once the whole thermal procedure is processed, both heat diffusion and Joule heating are fused together in heat conduction procedure and the separated pattern assembles less in the crack tips.

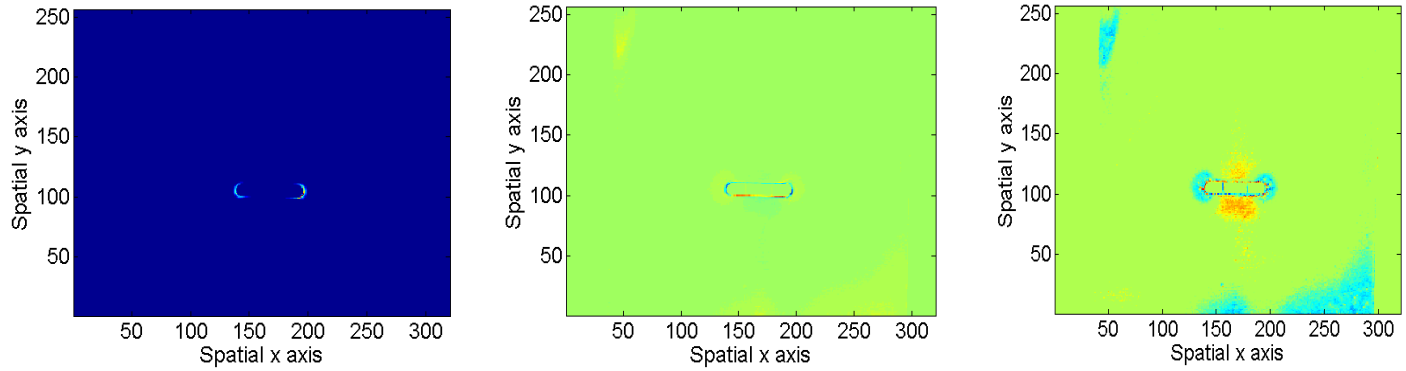

(a) (b) (c)

Fig. 7: Sparse pattern extraction results (A) the proposed method, (B) variational Bayesian sparse PCA with Gaussian sparse prior and (C) Bayesian sparse PCA based on Monte Carlo Markov Chain with Bernoulli sparse prio

B. Impact of Sparse Pattern extraction

The sparse pattern extraction takes important role in quantitatively analyzing the cracks. We have compared the proposed method with the relative recent approach on sparse pattern extraction. These are the variational Bayesian sparse PCA with Gaussian sparse prior [49] and the robust Bayesian PCA with Bernoulli sparse prior [50]. The comparison is validated in both accuracy and computation complexity. In our proposed method, the sparse greedy model is explored for sparse pattern extraction which by adjusting proper sparse parameters that even gives better results and behaves much faster update procedure. Fig. 7 shows the extraction results.

In Fig. 7, by emphasizing the sparseness of solution, the edge of the hot spots on crack tips can be quantified and has benefitted the quantitative sizing of the defect. The proposed method has successfully accentuate the expected sparse locations which indicate the hot spots of the crack tips. The variational Bayesian sparse PCA has also outlined the defect edge, however, with reference to the physics mechanism, the edges along the hot spots have been incorrectly detected (which should not present., Finally, the full Bayesian sparse PCA presents an inferior result which has emphasized both hot and cool areas as well as being interfered by noise. The above results are also confirmed by POD results as shown in Table II. The POD study is the comparison results between the referenced annotation with the extraction by algorithms. Fig. 8 shows the annotation results where the crack edge region is marked as "1" and the rest denoted as "0".

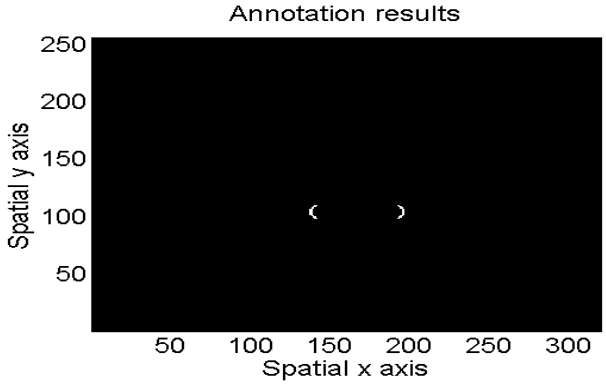

Fig. 8: Annotation results of crack edge

TABLE II
SSIM RESULTS OF DIFFERENT METHODS

Methods	POD	CPU time (s)
PCA of the whole video	0.84	169.5
PCA on phase one	0.91	15
Proposed method	0.99	3.5
VB Sparse PCA	0.87	7.64
MCMC Sparse PCA	0.68	1029

Table II shows the comparison of the proposed method based on phase one thermal sparse pattern extraction. With human annotation results, the POD for all different methods, while a higher performance is attained by the proposed method with an average accuracy of 99%.

The Variational Bayesian Sparse PCA (VBSPCA) gives 87% while the worst result is obtained by MCMC Sparse PCA which gives 68%. In addition, according to the computation time, the proposed method gives extremely low cost while it only take 0.07 seconds to achieve the extraction. This brings significantly benefits for industry online-detection. VBSPCA requires more time about 7.64 seconds and the MCMC Sparse PCA requires the most time about 1029 seconds. The reasons for these is attributed to both Variational Bayesian and fully MCMC Sparse PCA having to update the model parameters and hyperparameters in each iteration which cost extra computation complexity. Although the update parameters has advantages to bypass human intervention but it brings the drawbacks to the incorrect selection of prior distribution for the model parameters and/or convergence to local minima.

In terms of parameters selection of the proposed method, the parameter K and tolerance τ does not highly affect the extraction results. In general, it suffices to set $K=1$ and $\tau=10^{-3}$ and this has been validated using Monte-Carlo repeated experiment involving more than 100 independent trials. On the other hand, the sparse pattern extraction results is highly reliant on λ and Δr. Firstly, for determining λ, which is based on model order selection where experiment is repeated by progressively increasing λ from 0.1 to 1 with step size is 0.1 (the deviation of the performance of all three experiments is POD ± 0.015). Secondly, We have constructed another experiment by varying Δr. This parameter is a rank step size

and should be integer. Our approach to determining Δr is based on model order selection where experiment is repeated by progressively increasing Δr from 1 to 5. For each experiment, we record the POD results and the overall obtained result is shown in Figure 9. It is clearly seen from the figure the best POD result is obtained when $\Delta r = 2$. The POD results decrease gradually with the setting of $\Delta r > 2$.

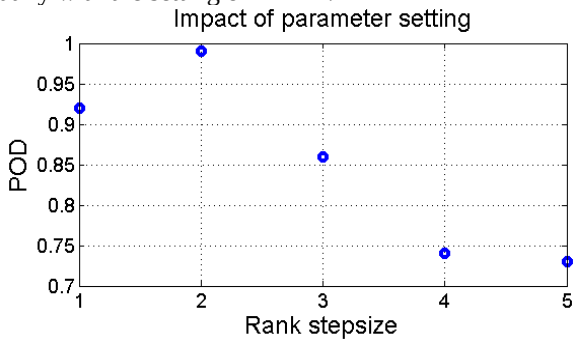

Fig. 9: the impact of parameter setting on POD results

C. Impact of detectability of contamination level of material

The measurement set-up variation, relative humidity of the room, contamination level of material are valuable for the practical application of inductive thermography. Among the above three impact factors, the contamination level on the surface is the main factor to interface the results. In order to validate the proposed method in this situation, we have done the extra experiment. In the in-situ application, the materials under test (MUT) always have oil, coating, or an oxidation layer on the surface. This will change the thermal emissivity significantly. The variation can be used to detect the surface damage like rust or corrosion. However, the variation sometimes introduces illusory temperature inhomogeneity and results in false alarms. We paint the sample surface with black and shine strips which are equally spaced with 5mm width. The shinning strips are the polished area while the black strips are the area sprayed with black paint. Both illustrate different level of emissivity. The emissivity of the black region is 1, which is the same for a blackbody. On the other hand, the emissivity of the shinning stainless steel surface is about 0.16. In this situation, once the test sample with the mixture of areas with strong emissivity gradient over another (e.g. black stains on the surface) and defect (e.g. slot which consists of cool and hot spots areas), the task of separating different thermal patterns becomes a very difficult challenge. Generally, the temperature of hot spots is three times higher than the cool area. However, the temperature of a black strip region can be as high as ten times higher than at the cool area due to the high emissivity. In this case, the hot spots around the slot tip cannot be observed and this directly reduces the probability of detecting the defects. Fig. 1b shows the temperature distribution at the end of heating (0.1s) of testing sample in Fig. 10a. Due to the high emissivity of the black area, there is no obvious high temperature region around the slot tips. The high temperature can only be observed at the black area above the coil. In addition, Fig. 10c shows the temperature distribution at the cooling phase (1.6s). The high temperature still can only be observed at the black strip area because of both high emissivity and heat diffusion. The transient temperature behavior at different positions is shown in Fig. 11. Pos 1 is at the crack side with black strip (high emissivity), Pos 2 is at the black strip where the area is far away from the excitation, Pos 3 is at the crack tip with the shinning strip, Pos 4 is at the crack side with shinning strip above the coil.

As can be seen in Fig. 11, different position behaves with different temperature transient characteristics. However, Pos 1 as well as other similar black strip area (above the coil) exhibits extreme high temperature transient in both heating and cooling phase in which other thermal patterns have been over-shadowed and therefore, they cannot be distinguished. This issue is difficult to tackle in defect detection using the ECPT method where the hot spot around defect tips cannot be taken as an indicator of defects especially for small cracks. Notwithstanding this, it will lead to error when both black stain and cracks are present on the surface of the test sample.

Thus the proposed method as well as compared methods will face a very challenging task to separate the hot spots. The following are the extraction results obtained from the proposed method, Variational Bayesian sparse PCA, MCMC Sparse Bayesian Sparse PCA, and general PCA.

TABLE III
SSIM RESULTS OF DIFFERENT METHODS

Methods	POD	CPU time (s)
Proposed method	0.97	5.5
VB Sparse PCA	0.91	8.34
MCMC Sparse PCA	0.63	1043
PCA on phase one	0.78	18

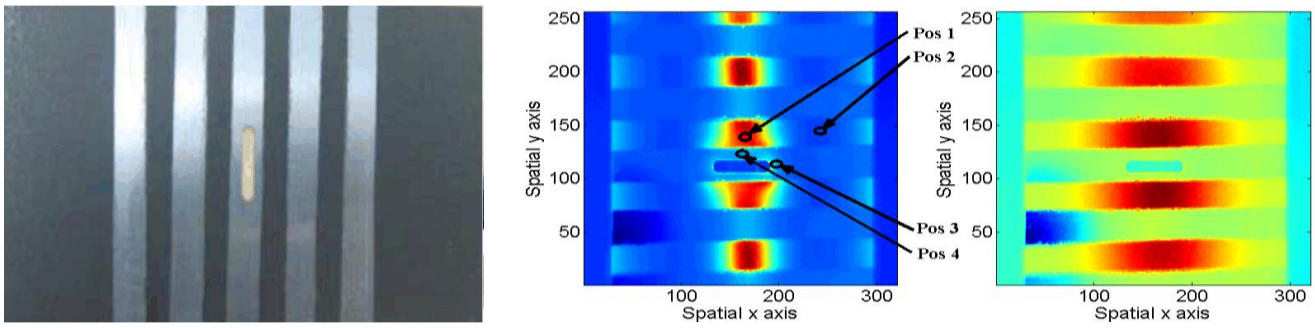

(a) (b) (c)

Fig. 10: (a) Painted steel sample with slot, (b) Infrared image at 0.1s (the end of heating phase) and (c) infrared image at 1.6s (the cooling phase)

Fig. 12 shows that by emphasizing the sparseness of solution, the edge of the hot spots on crack tips can be quantified at the situation even under the influence of various emissivity levels. The proposed method has successfully extracted the expected sparse locations that indicate the hot spots of the crack tips. The variational Bayesian sparse PCA has also accurately outlined the defect edge but it still mixes with the emissivity interface and misses the informative points of left edge. The full Bayesian sparse PCA performs less satisfactorily and still retains a mixture of a large part of ambiguity. Finally, the general PCA has enabled the extraction of the hot spots region but it has not fully reduced the emissivity interface. The above resultsare also supported by the POD results as shown in Table III. In terms of time consumption, the proposed method is very fast and takes only 0.11 second to render the extraction. The Variational Bayesian Sparse PCA also gives fast computation and takes about 8.34 second while the MCMC Sparse PCA as well as the general PCA take a relatively longer time and requires about 1043 second and 18 second, respectively.

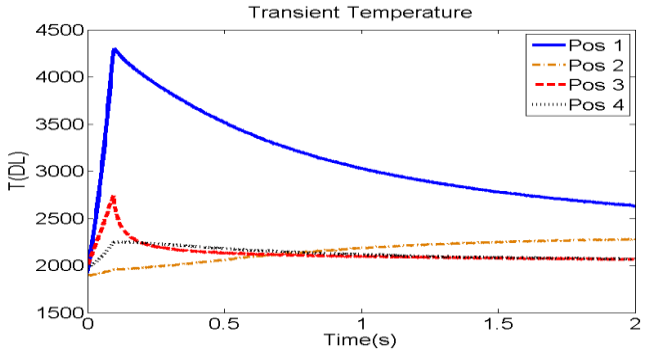

Fig. 11: Transient response of different positions

D. Industrial application: Micro-natural crack detection

To verify the proposed system, thermal fatigue cracks (a 4.2 mm length crack) in steel blade are used for testing. A steel blade sample provided by Alstom is also investigated in this study (Fig. 13 and Fig. 14). In the blade, flaws are produced in-situ with controlled thermal fatigue loading. The flaws grow with natural thermal fatigue damage mechanism. In this study, one natural crack: 167BBB1361 is detected. The crack location is marked with red circles in Fig. 13. Crack 167BBB1361 is 4.2 mm length. A 200 ms heating duration is selected for inspection.

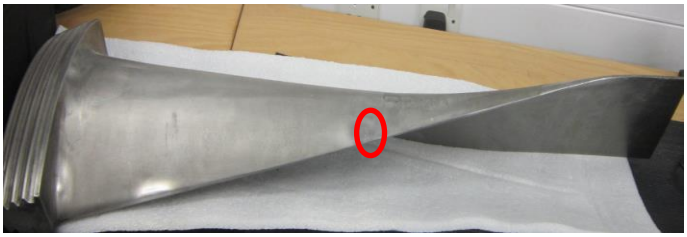

Fig. 13: Steel blade with thermal fatigue natural crack

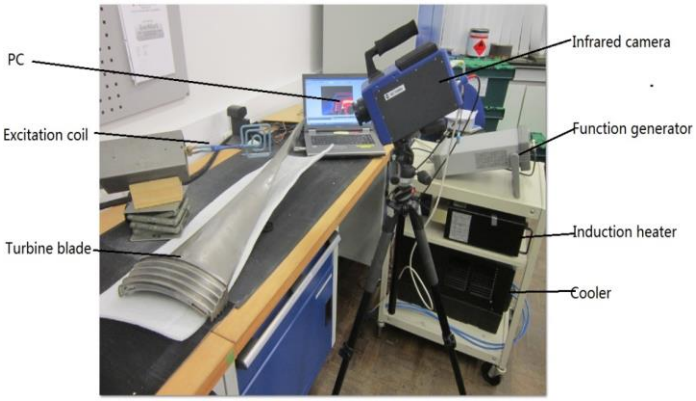

Fig. 14: ECPT test platform

Fig. 15 shows the general NDT method using Penetrant Test (PT) image provided by Alstom and ECPT image at 0.1 s. In the PT image, the area of cracks is marked with red circle. The hot spots of crack can be visually identified, while the image is blurred. This phenomenon indicates that there exist cracks in the sample. However, the cracks are difficult to be quantified. Fig. 16 shows the proposed results.

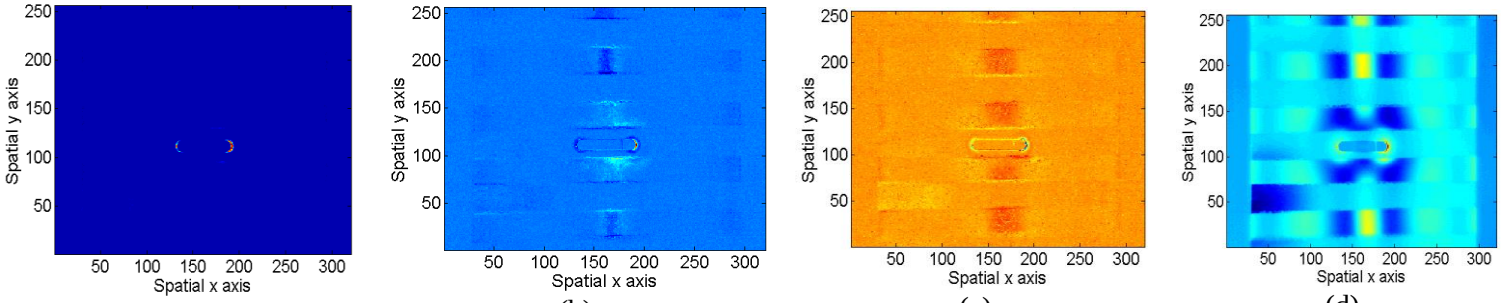

Fig. 12: Pattern extraction results (A) the proposed method, (B) variational Bayesian sparse PCA, (C) Bayesian sparse PCA based on Monte Carlo Markov Chain and (D) general PCA

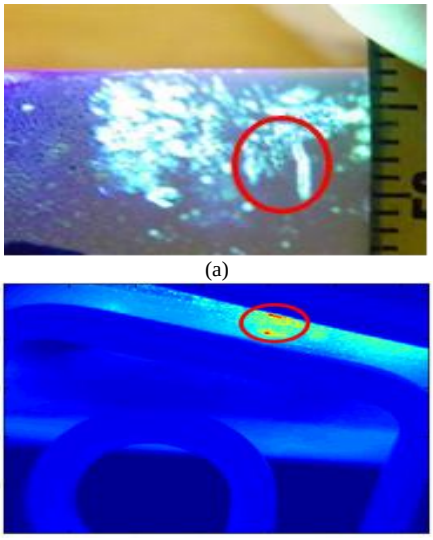

(a)

(b)

Fig. 15: Thermal fatigue natural cracks detection: length: 4.2 mm (a) PT image, (b) ECPT image at 0.1 s

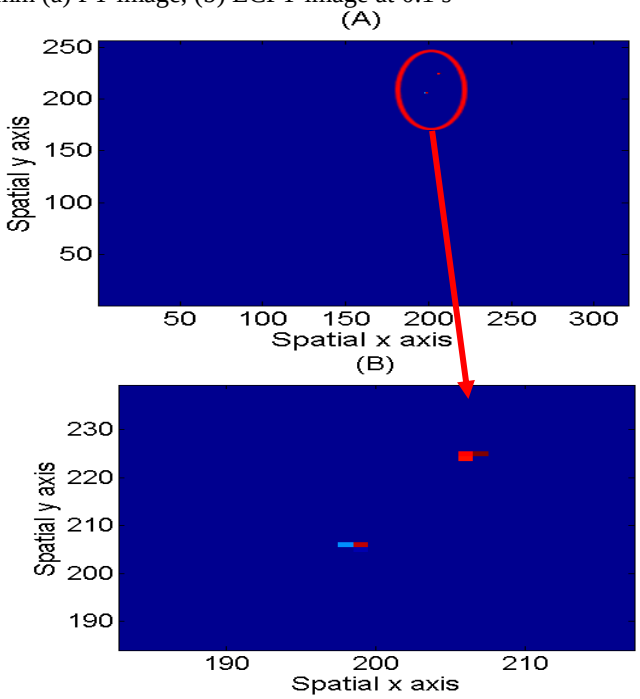

Fig. 16: (A) Thermal sparse pattern extraction results of natural crack. (B) Zoomed-in result (red circle)

From Fig. 16, it is clearly shown that the proposed method has not only accurately located the hot spots (crack tips) but also precisely sized the cracks. By comparing with human detection, the proposed method is a fully automatic and unsupervised defect detection method. The human detection seriously suffers from the lack of subjective evaluation and requires the manual selection of informative data for the defect detection. In addition, current defect characterization method in IT imaging system requires highly trained personnel. Therefore, automated defect characterization method is very desirable in future Intelligent Manufacturing and Maintenance. Moreover, the time cost is high since it requires manual detection. The detection results may not be repeatable. Additionally, considering the accuracy, this can be divided into two parts for comparison: standard defect sample and natural defect. The human detection can render reasonably good accuracy in evaluating the defect based on regular sample. This is very sensible since the defect itself is introduced by human and we have the prior knowledge of the location and size of the defect. For natural cracks, it is extremely difficult for human detection because all the prior knowledge is unknown and the cracks are significantly small. This is shown in Figure 13 where the size of the crack is only 1mm wide. This is a very difficult task for human to detect the natural crack.

The method (ECPT) is specific for conductive materials from carbon fibre reinforced plastic composites to metals, and multi-layer components including conductive parts. Its limitation is that it is invalid for non-conductive materials. However, by means of changing the inductive heater to lamp heater, ultrasound heater or laser heater, the proposed data analytics method and its physics interpretation are still valid for almost all thermal-conductive material.

VI. Conclusions and Future Work

In this paper, inductive phase thermal sparse pattern extraction has been proposed for NDT&E. Both ECPT system and algorithm have been tested to validate the method. The physic interpretation of heat conduction phase of both Joule heating and heat diffusion has been conducted and the phase of Joule heating proved its efficiency for crack detection. The sparse pattern extraction method allows and emphasis sparse abnormal pattern such as hot spots around the crack tips to be extracted automatically for flaw contrast enhancement. The proposed method has been tested on both man-made and natural defects from industry. Future work will focus on samples with complex surface condition, e.g. roughness and emissivity variation. Complexity defects detection, e.g. subsurface defect in metallic material, impact damage and delamination in carbon fiber structures will also be investigated.

V. Acknowledgement

The work was supported by National Natural Science Foundation of China (Grant No. 51377015 and No. 61401071), Supported by NSAF (Grant No. U1430115), FP7 HEMOW IRSES project 269202, China Postdoctoral Science Foundation (No.136413), the Science & Technology Department of Sichuan Province, China (Grant No. 2013HH0059), and the Fundamental Research Funds for the Central Universities (Grant No. ZYGX2014J068)

References

[1] H. Gao,C. Ding, C. Song, and J. Mei, "Automated Inspection of E-Shaped Magnetic Core Elements Using K-tSL-Center Clustering and Active Shape Models", *IEEE Trans. Ind. Informat.*, vol. 9, pp. 1782-1789, 2013

[2] W.C. Li and D.M. Tsai, "Defect Inspection in Low-Contrast LCD Images Using Hough Transform-Based Nonstationary Line Detection", *IEEE Trans. Ind. Informat.*, vol. 7, pp.136-147, 2011

[3] X.L. Bai, Y.M. Fang, W.S. Lin, L.P. Wang, B.F. Ju, "Saliency-based Defect Detection in Industrial Images by Using Phase Spectrum," *IEEE Trans. Ind. Informat , 2014*

[4] G. Acciani, G. Brunetti, and G. Fornarelli, "Application of neural networks in optical inspection and classification of solder joints in surface mount technology", *IEEE Trans. Ind. Informat.*, vol. 2, pp. 200-209, 2006

[5] D.-M. Tsai, I.-Y. Chiang, and Y.-H. Tsai, "A shift-tolerant dissimilarity measure for surface defect detection," *IEEE Trans. Ind. Informat.*, vol. 8, pp. 128–137, Feb. 2012

[6] A. Picon, O. Ghita, P. F. Whelan, and P. M. Iriondo, "Fuzzy spectral and spatial feature integration for classification of nonferrous materials in hyperspectral data," *IEEE Trans. Ind. Informat*, vol. 5, pp. 483–494, 2009.

[7] Y. Si, J. Mei, and H. Gao, "Novel approaches to improve robustness, accuracy and rapidity of iris recognition systems," *IEEE Trans. Ind. Informat*, vol. 8, pp. 110–117, Feb. 2012

[8] Bin Gao, Hong Zhang, W.L. Woo, Gui Yun Tian, Libing Bai, Aijun Yin "Smooth Nonnegative Matrix Factorization for defect detection using Microwave Non-destructive Testing and Evaluation" IEEE Transactions on Instrumentation and Measurement, vol.63, no.4, 923 – 934, 2014.

[9] D. M. Tsai and J. Y. Luo, "Mean shift-based defect detection in multicrystalline solar wafer surfaces," *IEEE Trans. Ind. Informat*, vol. 7, pp.125–135, Feb. 2011.

[10] X. P. Maldague, Theory and Practice of Infrared Technology for Nondestructive Testing, Wiley-Interscience, 2001

[11] Patrik Broberg. Surface crack detection in welds using thermography. NDT & E International, vol. 57, pp. 69-73, 2013.

[12] R Yang, Y He, Bin Gao, GY Tian, "Inductive pulsed phase thermography for reducing or enlarging the effect of surface emissivity variation", Applied Physics Letters 105 (18), 184103, 2014.

[13] Bin Gao, Aijun Yin, Guiyun Tian and W. L. Woo, "Thermography spatial-transient-stage mathematical tensor construction and material property variation track", *International Journal of Thermal Sciences*, vol. 85, pp. 112-122, 2014

[14] Hailong Yang, Bin Gao, Guiyun Tian, Wenwei Ren, Wai Lok Woo, "Transient-Spatial Pattern Mining of Eddy Current Pulsed Thermography Using Wavelet Transform", CHINESE JOURNAL OF MECHANICAL ENGINEERING, vol. 27, no.4, pp. 768-778, 2014.

[15] B. Oswald-Tranta and G. Wally, "Thermo-inductive surface crack detection in metallic materials," in Proc. 9th Eur. Conf. NDT, Berlin, Germany, 2006, paper We.3.8.3.

[16] G Zenzinger, J Bamberg, W Satzger, V Carl, "Thermographic crack detection by eddy current excitation," *NDT&E International*, vol. 22, no. 2-3, pp. 101-111, 2007.

[17] B Weekes, D P Almond, P Gawley, T Barden, "Eddy-current induced thermography-probability of detection study of small fatigue cracks in steel, titanium and nickel-based superalloy," *NDT&E International*, vol. 49, pp. 47-56, 2012.

[18] Y. He, G. Tian, M. Pan et al., "Impact evaluation in carbon fiber reinforced plastic (CFRP) laminates using eddy current pulsed thermography," Composite Structures, vol. 109, pp. 1-7, 2014

[19] Y. He, G.Y. Tian, M. Pan, D. Chen, H. Zhang, "An investigation into eddy current pulsed thermography for detection of corrosion blister, Corrosion Science", vol.78, pp.1-6, 2014

[20] J Wilson, G Y Tian, I Mukriz, D Almond, "PEC thermography for imaging multiple cracks from rolling contact fatigue," *NDT&E International*, vol. 44, pp. 505-512, 2011.

[21] Liang Cheng, Bin Gao, Gui Yun Tian,W.L. Woo, and G. Berthiau, "Impact Damage Detection and Identification using Eddy Current Pulsed Thermography through Integration of PCA and ICA", IEEE Sensors Journal, vol.14, no. 5, 2014.

[22] X Maldague, S Marinetti, "Pulse phase infrared thermography," *J. Appl Phys.*, vol. 79, no. 5, pp. 2694-8, 1996.

[23] K Chatterjee, S Tuli, "Image enhancement in transient lock-in thermography through time series reconstruction and spatial slope correction," *IEEE Trans. Instrument and Measurement*, vol. 61, no. 4, pp. 1079-1089, 2012

[24] S Marinetti, E Grinzato, P G Bison, E Bozzi, M Chimenti, G Pieri, O Salvetti, "Statistical analysis of IR thermographic sequences by PCA," *Infrared Physics & Technology*, vol. 46, pp, 85-91, 2004.

[25] A. Hyvarinen, J. Karhunen, and E. Oja, "Independent component analysis and blind source separation," John Wiley & Sons, pp.20–60, 2001

[26] Bin Gao, Libing Bai, Gui Yun Tian, W.L. Woo, Yuhua Cheng "Automatic defect identification of eddy current pulsed thermography using single channel blind source separation*" IEEE Trans. Instrument and Measurement*, vol.63, no.4, pp.913-922. 2014.

[27] C. Févotte, "Majorization-minimization algorithm for smooth Itakura-Saito nonnegative matrix factorization," in *Proc. of IEEE International Conference on Acoustics, Speech and Signal Processing* (ICASSP), pp. 1980-1983, 2011

[28] Bin Gao, Libing Bai, W. L. Woo, and Guiyun Tian, "Thermography pattern analysis and separation", *Applied Physics Letters*, 104, 251902; doi: 10.1063/1.4884644, 5 pages, 2014.

[29] M. Elad, Sparse and Redundant Representations: From Theory to Applications in Signal and Image Processing. Springer, 2010.

[30] J.-L. Starck, F. Murtagh, and J. Fadili, Sparse Image and Signal Processing: Wavelets, Curvelets, Morphological Diversity. Cambridge, 2010.

[31] E. Cand`es and M. Wakin, "People hearing without listening: An introduction to compressive sampling," IEEE Signal Processing Magazine, March 2008, 21–30.

[32] M. J. Fadili, J.-L. Starck, and F. Murtagh, "Inpainting and zooming using sparse representations," The Computer Journal, vol. 52, 2009, 64–79.

[33] Zechao Li, Jing Liu, Yi Yang, Xiaofang Zhou and Hanqing Lu, "Clustering-Guided Sparse Structural Learning for Unsupervised Feature Selection", IEEE Trans. Knowledge and Data Engineering (TKDE), vol. 26, no.9, pp. 2138 – 2150, 2014.

[34] Bin Gao, W.L. Woo, S.S. Dlay, "Variational Bayesian Regularized Two-Dimensional Nonnegative Matrix Factorization", IEEE Trans. on Neural Networks and Learning Systems, vol. 23, pp. 703-716, 2012.

[35] Bin Gao, W.L. Woo, S.S. Dlay, "Adaptive Sparsity Non-negative Matrix Factorization for Single Channel Source Separation", IEEE Journal of Selected Topics in Signal Processing, vol. 5, pp. 1932-4553, June 2011.

[36] Bin Gao, W.L. Woo and S.S. Dlay, "Unsupervised Single Channel Separation of Non-Stationary Signals using Gammatone Filterbank and Itakura-Saito Nonnegative Matrix Two-Dimensional Factorizations", IEEE Trans. Circuits and Systems I, vol. 60, no. 3, pp. 662-675, 2013.

[37] J.-L.Starck, J.Fadili, and F.Murtagh, "The undecimated wavelet decomposition and its reconstruction," IEEE Trans. on Image Processing, vol. 16, pp. 297–309, 2007.

[38] M. J. Fadili and J.-L. Starck, "Curvelets and ridgelets," in Encyclopedia of Complexity and System Science. Springer, 2008, in press.

[39] M. Aharon, M. Elad, and A. Bruckstein, "K-SVD: An algorithm for designing overcomplete dictionaries for sparse representation," ITSP, vol. 54, no. 11, 2006, 4311–4322.

[40] M. Zibulevski, "Blind source separation with relative Newton method," in Proc. of ICA, Independent Component Analysis, 2003, 2003, 897-902.

[41] J. Kruskal, "Greedy algorithm for the minimum spanning tree problem", Proceedings of the American Mathematical Society, 1956, pp. 48-50.

[42] K. Papadimitriou and K. Steiglitz, Combinatorial Optimization: Algorithms and Complexity. Prentice-Hall, Englewood Cliffs, NJ, 1982.

[43] J. Tropp and A. Gilbert, "Signal recovery from random measurementsvia orthogonal matching pursuit," IEEE Trans. Inf. Theory, vol. 53, no.12, pp. 4655–4666, Dec. 2007.

[44] D. Needell and R. Vershynin, "Uniform uncertainty principle and signal recovery via regularized orthogonal matching pursuit," Found. Comput. Math., vol. 9, no. 3, pp. 317–334, June 2009.

[45] Bin Gao, W.L. Woo and L.C. Khor, "Cochleagram-Based Audio Pattern Separation Using Two-Dimensional Non-Negative Matrix Factorization With Automatic Sparsity Adaptation," J. Acoust. Soc. Am., vol. 135, no. 3, pp. 1171-1185, 2014

[46] N. Tengtrairat, Bin Gao, W.L. Woo and S.S. Dlay, "Single-channel blind separation using pseudo-stereo mixture and complex 2-D histogram," IEEE Trans. on Neural Networks and Learning Systems, vol. 24, no. 11, pp. 1722-1735, 2013.

[47] J. Bobin, J.-L. Starck, M. J. Fadili, and Y. Moudden, "Sparsity and morphological diversity in blind source separation," IEEE Trans. on Image Processing, vol. 16, no. 11, 2007, 2662–2674.

[48] E. J.Candès,X.Li, Y.Ma, and J.Wright, "Robust principal component analysis?," CoRR, vol. abs/0912.3599, 2009

[49] Z. Lin, A. Ganesh, J.Wright, L.Wu, M. Chen, and Y. Ma, "Fast convex optimization algorithms for exact recovery of a corrupted low-rank matrix," SIAM J. Optimiz., 2009, submitted for publication

[50] S.D. Babacan, M. Luessi, R. Molina, A.K. Katsaggelos, "Sparse Bayesian Methods for Low-Rank Matrix Estimation", IEEE Transactions on Signal Processing, vol.60, no.8, pp. 3964 – 3977, 2012.

[51] X. Ding, L. He and L. Carin, "Bayesian robust principal component analysis," IEEE Trans. Image Processing, vol. 20, pp. 3419-3430, 2011.
[52] Y. He, M. Pan, D. Chen, G. Tian, H. Zhang, "Eddy current step heating thermography for quantitatively evaluation", Applied Physics Letters, 103 (2013) 194101, 2013
[53] Aijun Yin, Bin Gao, Gui Yun Tian, W.L. Woo, Kongjing Li "Physical interpretation and separation of eddy current pulsed thermography", *Journal of Applied Physics* vol. 113, 064101, doi: 10.1063/1.4790866, 2013
[54] Bin Gao, W.L. Woo and Bingo W-K. Ling, "Machine learning source separation using maximum a posteriori nonnegative matrix factorization," IEEE Trans. on Cybernetics, vol. 44, no. 7, pp. 1169-1179, 2014.
[55] B. Gao, W.L. Woo, S.S. Dlay, "Single channel source separation using EMD-subband variable regularized sparse features," *IEEE Trans. on Audio, Speech and Language Processing*, vol. 19, pp. 961-976, 2011
[56] Demmel, James; Kahan, William, "Accurate singular values of bidiagonal matrices, " Society for Industrial and Applied Mathematics. *Journal on Scientific and Statistical Computing*, vol. 11, pp. 873–912, 1990
[57] J. Tropp, A. Gilbert, M. Strauss, "Algorithms for simultaneous sparse approximations – Part I: Greedy pursuit", *Signal Processing*, vol.86, pp 572–588, 2006.
[58] Tianyi Zhou and Dacheng Tao, "Greedy bilateral sketch, completion & smoothing", in Proc. of 2013 JMLR Workshop and Conference, vol. 31. pp. 650–658.
[59] Z. Wang, A. C. Bovik, H. R. Sheikh, and E. P. Simoncelli, "Image quality assessment: From error visibility to structural similarity," *IEEE Trans. Image Processing*, vol. 13, no. 4, pp. 600-612, Apr. 2004.

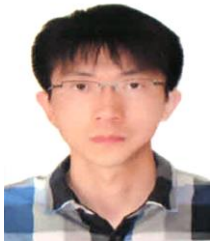

Bin Gao (M' 12-SM' 14) received his B.S. degree in communications and signal processing from Southwest Jiao Tong University (2001-2005), China, MSc degree in communications and signal processing with Distinction and PhD degree from Newcastle University, UK (2006-2011). He worked as a Research Associate (2011-2013) with the same university on wearable acoustic sensor technology. Currently, he is an Associate Professor with the School of Automation Engineering, University of Electronic Science and Technology of China (UESTC), Chengdu, China. His research interests include sensor signal processing, machine learning, social signal processing, nondestructive testing and evaluation where he actively publishes in these areas. He is also a very active reviewer for many international journals and long standing conferences. He has coordinated several research projects from National Natural Science Foundation of China

Wai Lok Woo (M'09–SM'11) received his BEng degree (1st Class Hons.) in Electrical and Electronics Engineering and the PhD degree from the Newcastle University, UK. He was awarded the IEE Prize and the British Scholarship to continue his research work. He is currently a Senior Lecturer and Director of Operations with the School of Electrical and Electronic Engineering. His major research is in the mathematical theory and algorithms for nonlinear signal and image processing. This includes areas of machine learning for signal processing, data mining, blind source separation, multidimensional signal processing, and high performance computational intelligence. He has an extensive portfolio of relevant research supported by a variety of funding agencies. He has published over 250 papers on these topics on various journals and international conference proceedings. Currently, he is Associate Editor of several international journals and has served as lead-editor of journals special issues. Dr Woo is a Senior Member of the IEEE and a Member of the Institution Engineering Technology (IET).

Yunzhe He (M'11) is a lecturer in National University of Defense Technology (NUDT), China, He finished the Joint PhD study at School of Electrical, Electronic Engineering, Newcastle University, UK and National University of Defense Technology, China in February, 2012. He got the PhD degree at College of Mechatronics Engineering and Automation, National University of Defense Technology (NUDT) in December, 2012. His research is focused on eddy current testing, thermography, and composite testing in the field of Non-destructive testing (NDT) and Structural health monitoring (SHM). In recent 5 years, he has chaired or participated in about 20 projects including NSFC, EPSRC etc. And he has published more than 40 academic papers in journals and conferences, which have been cited more than 500 times in Google scholar and the h-index is 12.

Gui Yun Tian (M'01–SM'03) received the B.Sc. degree in metrology and instrumentation and M.Sc. degree in precision engineering from the University of Sichuan, Chengdu, China, in 1985 and 1988, respectively, and the Ph.D. degree from the University of Derby, Derby, U.K., in 1998. From 2000 to 2006, he was a Lecturer, Senior Lecturer, Reader, Professor, and Head of the group of Systems Engineering, respectively, with the University of Huddersfield, U.K. Since 2007, he has been based at Newcastle University, Newcastle upon Tyne, U.K., where he has been Chair Professor in Sensor Technologies. Currently, He is also with School of Automation Engineering, University of Electronic Science and Technology of China. He has coordinated several research projects from the Engineering and Physical Sciences Research Council (EPSRC), Royal Academy of Engineering and FP7, on top of this he also has good collaboration with leading industrial companies such as Airbus, Rolls Royce, BP, nPower and TWI among others.